Journal of Membrane Science 636 (2021) 119548

Contents lists available at ScienceDirect

Journal of Membrane Science

journal homepage: www.elsevier.com/locate/memsci

Mechanistic insights into flow-dependent virus retention in different nanofilter membranes

Remo Leisi [a,*], Eleonora Widmer [b], Barry Gooch [c], Nathan J. Roth [b], Carlos Ros [a]

[a] Department of Chemistry and Biochemistry, University of Bern, Freiestrasse 3, 3012, Bern, Switzerland
[b] CSL Behring AG, Wankdorfstrasse 10, 3000, Bern, 22, Switzerland
[c] CSL Behring, 1st Ave 1020, 19406, King of Prussia, PA, USA

ARTICLE INFO

Keywords:
Virus filtration
Parvovirus retention
Pressure release
Membrane structure
Flow interruption

ABSTRACT

Virus filtration is a downstream unit operation in the manufacturing of biotherapeutics to remove potential viral contaminations based on size exclusion. While even very small viruses are effectively retained under normal flow conditions, process interruptions can compromise the virus-reduction capacity of a filter. Yet, direct insights into the underlying flow-dependent retention and breakthrough mechanisms of relevant parvoviruses are still lacking. To study the retention of parvoviruses inside the polymeric structures of four commonly used filter types, minute virus of mice (MVM) was fluorescently labeled and visualized in membrane cross-sections post-filtration by laser scanning microscopy. The virus retention profiles revealed a membrane structure-specific accumulation of viral particles at a distinct depth in the separation-active layers. Pressure release experiments showed that flow interruption-induced virus breakthrough is associated with the mobilization and deeper migration of viruses into denser membrane layers. Moreover, we discovered that local clusters of breakthrough foci in a particular filter type are responsible for the substantial transmission of viruses to the filtrate. Taken together, the membrane-specific phenomena visualized herein contribute to a better understanding of the underlying virus retention mechanisms and provide cues for a specific optimization of virus filtration processes.

1. Introduction

Biotherapeutics, such as monoclonal antibodies (mAbs) or plasma-derived medicinal products (PDMPs), originate from biological sources, which carry an inherent risk of viral contamination. Mammalian cell cultures commonly used to produce recombinant proteins are known to endogenously express retrovirus-like particles [1]. Additionally, cell cultures might be infected by adventitious viruses introduced into the manufacturing process, for examples by raw materials. Contamination of bioreactors with minute virus of mice (MVM) for instance has repeatedly caused production failures and significant economic losses [2–4]. The starting material for the manufacture of PDMPs, human plasma, may contain viral agents despite rigorous selection of donors, as well as testing of donations and plasma pools for the absence of relevant blood-borne viruses [5,6]. Thus, to further assure the safety of biological therapeutics, manufacturers incorporate dedicated virus inactivation and removal steps in a downstream purification process to effectively eliminate any infectious viral entities that could potentially enter the manufacturing process [7].

Virus filtration is considered one of the most effective, robust, and broadly applicable virus clearance tools, as it removes viral contaminants based on a size-exclusion mechanism [8,9]. Virus filter membranes consist of polymers like regenerated cellulose (RC), poly (vinylidene fluoride) (PVDF) or polyether sulfone (PES), which form an interconnected structure of nanoscale voids and capillaries. The membranes are designed to have sufficiently small pore sizes (generally 18–20 nm) to assure that even the smallest known relevant viruses are retained while most therapeutic molecules can easily pass through.

Due to their small size, parvoviruses (e.g. MVM) are used as worst-case virus models for the validation of virus filtration applications in biomanufacturing processes [10,11]. The outer capsid diameter of parvoviruses has accurately been determined by X-ray crystallography and CryoEM to be 27–29 nm [12–15]. As such, small-pore virus filters are capable of effectively retaining parvoviruses based on their size under typical operating conditions. Nevertheless, there are manufacturing process parameters that are known to be critical to maintaining the integrity of virus filtration.

For example, deviations from the normal filtration flow due to filter fouling-induced flux decay or pressure release events have been shown

* Corresponding author.
E-mail address: remo.leisi@dcb.unibe.ch (R. Leisi).

https://doi.org/10.1016/j.memsci.2021.119548
Received 22 April 2021; Received in revised form 17 June 2021; Accepted 20 June 2021
Available online 26 June 2021

Abbreviations

B19V	parvovirus B19
CF	constant flow
dpi	days post-infection
DOL	degree of labeling
EM	electron microscopy
FI	flow interruption
LSM	laser scanning microscopy
LRV	logarithmic reduction value
MVM	minute virus of mice;
NHS-Atto	N-hydroxy-succinimide ester-modified Atto dye
PBS	phosphate buffered saline;
PDMPs	plasma-derived medicinal products
PES	polyether sulfone
PPV	porcine parvovirus
PSD	pore size distribution
PSG	pore size gradient
PVDF	poly(vinylidene fluoride)
qPCR	quantitative polymerase chain reaction
RC	regenerated cellulose
RFU	relative fluorescence unit
SDS-PAGE	sodium dodecyl sulfate polyacrylamide gel electrophoresis
TEM	transmission electron microscopy
VLP	virus-like particle
VRP	virus retention profile.

to negatively impact the retention capability of virus filters [16–20]. The hydrodynamic force of the constant convective flow is thought to prevent lateral movement of viruses within the porous network by constraining the viral particles in retentive voids. During flow interruptions (FIs) or low flow conditions, however, the Brownian motion of viral particles resumes in all directions, raising the probability that viruses laterally pass through larger pores and potentially reach non-retentive pathways [21]. With the restart of the flow, these viral particles can migrate deeper into the separation-active layer (SAL) or even break through into the filtrate [19]. This diffusion-based model is supported by results demonstrating a significant impact of the solution viscosity and the duration of FI on the retention capacity of the filter [21,22].

In principle, virus filters are manufactured such that a large majority of the pores are smaller than the diameter of the virus, allowing for retention of viruses via a multi-step sieving process [21]. The maximal pore size – defined as the diameter where 99% of the pores are smaller - is as a reliable predictor of the virus retention capacity [23,24]. In second-generation filter types, reducing the maximal pore size by creating a more uniform pore size distribution (PSD) in the SAL has improved the filter performance and robustness, particularly during FIs or low flow conditions when compared to earlier filter generations [21, 25–27]. However, it should be noted that the flow-dependent virus breakthrough considerably depends also on the product feedstream and filter type used [18,22,27–29], as well as filtration conditions, such as pH and conductivity [27,29].

To investigate the diffusion-based retention model in more detail and to better understand the influence of specific operating conditions in the context of the individual filter morphologies, the direct visualization of viral particles inside the filter membranes is a valuable complementary approach to the conventional techniques [30,31]. Studies using fluorescently labeled bacteriophages as models for parvoviruses and detection by laser scanning microscopy (LSM) have suggested an internal polarization model in which viruses pass through the reservoir zone of the SAL until being rejected by membrane layers constituting pore sizes significantly smaller than the viral diameter [30,32]. Upon FI, the labeled bacteriophages migrated deeper into the rejection zone, correlating with an observed decay in virus retention [19]. Several follow-up studies used fluorescently-labeled nanospheres and gold particles to further characterize the SALs inside the intricate pore structure of different filter membranes and to visualize the impact of particular process conditions [24,33–37].

Bacteriophage models and artificial particles are valuable tools to explore the general principles of underlying retention mechanisms. However, similarly sized particles and viruses are known to occasionally exhibit considerable differences in virus filtration experiments [11,16, 25,38–40]. Therefore, conclusions based on non-relevant surrogates should to be verified by the parvovirus models used in virus filtration validation studies.

The aim of this work was to provide first mechanistic insights into the flow-dependent retention of a relevant parvovirus in various filter brands. To this end, Atto-633 labeled MVM was filtered under constant and interrupted flow conditions and subsequently localized by LSM in the filter membranes post-filtration. The visualization and precise determination of the virus retentions profiles (VRPs) inside the characteristic membrane morphologies confirmed several previous observations, but also revealed novel filter-specific phenomena.

2. Materials and methods

2.1. Cells and viruses

The minute virus of mice prototype (MVMp) clone commonly used in validation studies for virus reduction steps was obtained from the ATCC (USA) [41]. A plasmid encoding the bacteriophage MS2 coat protein for the expression of recombinant MS2 virus-like particles (VLPs) was cloned with a sequence obtained from GenScript (China) [42]. Mouse A9 fibroblasts derived from ATCC were cultured in Dulbecco's modified Eagle's medium (DMEM), 5% fetal calf serum (FCS) at 37 °C, 5% CO_2. Competent BL21(DE3) *E. coli* cells were obtained from Qiagen (Germany) and cultured in lysogeny broth medium.

2.2. Generation of MVM and MS2 VLPs

Propagation of MVM and expression of MS2 VLPs were performed as previously described [40]. Briefly, mouse A9 fibroblasts cells were inoculated with MVM and harvested 3 days post-infection (dpi) before extensive virus-induced cell lysis. Cells were repetitively washed with phosphate-buffered saline (PBS) and then lysed in PBS by three freeze-thaw cycles. The lysate was clarified by centrifugation at 3000×*g* for 10 min at 4 °C, and incubated with 0.1% Nonidet-P40 (NP-40) for 1 h at 4 °C. To express MS2 VLPs, BL21(DE3) cells transformed with the MS2 coat protein expression plasmid were selected by ampicillin resistance, grown to an optical density (OD_{600}) of 0.4, and induced with 1 mM isopropyl-β-D-thiogalactopyranoside (IPTG) for 16 h. Collected cell pellets were lysed in PBS by three freeze-thaw cycles, followed by sonication on ice (15 × 10 s). The cell lysate was clarified by centrifugation at 10,000×*g* for 30 min at 4 °C.

2.3. Purification of native MVM and MS2 VLPs

The clarified cell lysates containing MVM or MS2 VLPs were passed through 0.45 μm and 0.22 μm filters, and layered on a two-fold volume of 20% sucrose in PBS, 1 mM $MgCl_2$, 0.1% NP-40 provided in an OptiSeal Tube (Beckman Coulter, USA). The viral particles were pelleted by ultracentrifugation at 150,000×*g* for 3 h at 4 °C in a Ti70 rotor (Beckman Coulter). The supernatant was carefully removed to avoid

contamination of lower fractions. The pellet was resuspended in a small volume of the bottom fraction, diluted with PBS (1:1) and analyzed for yield and purity (Supplementary Fig. 1).

2.4. Quantification of viral capsids

To evaluate the total number of viral capsids, virus proteins were quantified by absorption at 280 nm (A_{280}) using the NanoDrop spectrophotometer (ThermoFisher, USA) and densitometric analysis of Coomassie-stained sodium dodecyl sulfate polyacrylamide gel electrophoresis (SDS-PAGE) using a known bovine serum albumin (BSA) concentration as reference for calibration.

2.5. Labeling of viruses with amine-reactive atto dyes

Suspensions containing viral particles were adjusted to 0.2–1 mg/mL virus protein in PBS, pH 7.4 and incubated with 70 μM of amine-reactive N-hydroxy-succinimide ester-modified Atto dyes (NHS-Atto; Atto-Tec, Germany) for 1 h at room temperature (RT) and overnight at 4 °C. To quench the crosslinking reaction, 50 mM Tris-HCl, pH 8, was added for 15 min at RT. Labeled virions were purified by ultracentrifugation through a 20% sucrose cushion in PBS, 1 mM $MgCl_2$ at 150,000×*g* for 3 h at 4 °C in a TLA 100.3 rotor (Beckman Coulter). The degree of labeling (DOL) was analyzed by comparison of the absorption of the labeled viruses at A_{280} against the maximal absorption (A_{max}) of the fluorescent dye [43]. MVM was labeled with Atto-633 dye, which was selected in our previous study as the preferred dye to minimally affect virus retention [40]. MS2 VLPs were labeled with Atto-488, which exhibits a slightly stronger but still minor effect on the retention, thus expectedly obtaining a similar retention as MVM. Labeling was performed to attain a limited DOL of about 25 dyes per capsid and thus to achieve a reasonable compromise between sufficient signal and negligible impact on the retention profile (Supplementary Table 1).

2.6. Dynamic light scattering of purified viruses

To confirm the monodispersity of virus preparations by dynamic light scattering (DLS), the virus suspensions were further purified to remove potentially interfering additives. Virus samples were diluted 1:10 in PBS and concentrated three times by 100 kDa cutoff Amicon Ultra centrifugal filter units (Merck Millipore, USA). Purified samples were incubated for 1 min in a sonication bath, passed through a 0.1 μm filter and analyzed using the Zetasizer Nano S instrument (Malvern Instruments, UK) at 25 °C (Supplementary Fig. 1, Supplementary Table 1).

2.7. Nanofiltration of Atto-labeled viruses in different filter types

Virus filtration experiments were performed with Planova 20N (Asahi Kasei, Japan), Pegasus SV4 (Pall Corporation, USA), Viresolve Pro (Merck Millipore), and Virosart HC (Sartorius, Germany) filters (Supplementary Table 2), using commercially available small-scale filter membranes derived from the same production lot. Unless indicated, virus filtration was carried out under standard operating conditions at room temperature (21–25 °C) and constant pressure following the manufacturer's instructions (Supplementary Table 3). The filter flow complied with specifications and membrane integrity tests passed in all shown experiments. A feedstream volume of 26 mL PBS was spiked with 1 μg of viral capsids, corresponding to 1.5×10^{11} MVM particles or 2.4×10^{11} MS2 VLPs, and passed through a 0.1 μm PVDF filter (Merck Millipore). All experiments were performed with spiking amounts significantly below the capture capacity of the filter, thus not influencing the filter flow, LRVs, or retention profiles of co-spiked viruses (Fig. 3, Supplementary Fig. 3) [39,40]. For analysis of viral load reduction, a feed sample (0.5 mL) and five filtrate fractions were collected (5 × 5 mL). Filtration was performed until the feed volume passed and flow stopped upon air contact (integrity test).

2.8. Preparation of membrane cross-sections for LSM

Due to various formats and properties, the different filter types necessitated preparation by an individual protocol. Except for Pegasus SV4 flat sheet membranes, Planova 20N, Viresolve Pro and Virosart HC filters were delivered in capsules, which were opened at the edges post-filtration by using a modified soldering bolt (300 °C tip). Pegasus SV4, Viresolve Pro and Virosart HC membranes were dried overnight at RT and embedded in paraffin. The embedded membranes were cross-sectioned (15 μm) orthogonally to the filtration direction using a Microm HM 355S (Histocom AG, Switzerland) and mounted on microscope glass slides (Greiner Bio-One, Austria). The Planova 20N membranes are specified to remain constantly wetted since drying of the hollow fiber leads to substantial contraction of the regenerated cellulose polymer. Therefore, to ensure membrane integrity post-filtration, a bundle of hollow fibers was embedded in 2% low EEO agarose (PBS), cross-sectioned by using a razor blade, and mounted with a drop of PBS, 10% glycerol atop a CELLview slide (Greiner Bio-One).

2.9. Determination of the virus retention profiles (VRPs) using laser scanning microscopy (LSM)

The mounted membrane cross-sections were analyzed using the laser scanning microscope 880 with a 63 × magnification objective (Carl Zeiss, Germany) and a drop of 80% glycerol for immersion. Lasers were run at 4% transmission and detector gain was set using the range indicator to establish an appropriate signal-to-noise ratio. The membrane cross-sections were scanned in a single stack using an averaged bi-directional scan, 16-bit depth, and a scan speed of 2. To visualize filter dimensions and stucture, the membrane autofluorescence was detected at λ_{ex} 405 nm; λ_{em} 422 nm. This excitation/emission settings provided significant intrinsic fluorescence of the cellulose-based membranes [44], and was found to be also suitable for the filters consisting of PES and PVDF, which both exhibited detectable autofluorescence at different UV wavelengths (data not shown). For 3D scans of the Pegasus SV4 membrane layers using 10 × and 20 × magnification objectives, one optical section per 1.5–2 μm and a scan speed of 9 were set. In this case, membrane dimensions were determined at λ_{ex} 425 nm; λ_{em} 485 nm to achieve a deeper laser penetration. Acquired data was processed with the ZEN program (Carl Zeiss) and exported as TIFF files. Images of membrane segments ($n \geq 3$) were analyzed with the ImageJ program [45] and the generated data was processed with GraphPad Prism to obtain retention profiles with confidence intervals as a function of the filter depth.

2.10. Quantitative analysis of virus signal in Pegasus SV4 membrane layers

Filter areas of 1 mm^2 area were scanned with a 10 × objective, consistently acquiring signal of the entire membrane depth to exclude a potentially biased detection due to membrane deformations. The combined stacks were analyzed by the ImageJ program, quantifying individual pixel intensities and calculating overall and local signal distributions. To resolve FI-induced breakthrough signals over a 2-log range, the data acquisition and processing settings were adjusted to obtain pixel intensities of 0.9–1 relative fluorescence units (RFU) for the retained signal in the first layer and about 0.01 RFU for the signal in the second layer after CF (Supplementary Fig. 10A).

2.11. Analysis of virus filter membranes by transmission electron microscopy (TEM)

Pieces of the membranes were embedded in Epon (Fluka, Switzerland) and left to harden at 60 °C for 5 days. Sections were produced with an ultramicrotome UC6 (Leica Microsystems, Austria), first semithin sections (1 μm) for light microscopy, which were stained with

a solution of 0.5% toluidine blue O (Merck, Germany) and then ultrathin sections (75 nm) for electron microscopy. The sections, mounted on single slot copper grids, were stained with UranyLess (Electron Microscopy Sciences, USA) and lead citrate with an ultrostainer (Leica Microsystems, Austria). Sections were examined with a transmission electron microscope (Tecnai Spirit, FEI, Czech Republic) equipped with a digital camera (Veleta, Olympus, Soft Imaging System, Germany).

2.12. Quantification of parvovirus reduction by qPCR

The concentration of MVM virions in the feed and filtrate fractions was determined by an optimized quantitative polymerase chain reaction (qPCR) protocol including a nuclease treatment before DNA extraction as previously described [40,46,47]. Nuclease treatment was performed with 4000 U/mL micrococcal nuclease (New England Biolabs, USA) in the manufacturer's 1 × nuclease buffer, 1 × BSA and additional 10 mM $CaCl_2$ for 30 min at 37 °C. EDTA (20 mM) was added to stop the nuclease digestion and to resolve calcium phosphate precipitations. Viral DNA was extracted (DNeasy Blood and Tissue Kit; Qiagen) and quantified by qPCR using the Luna qPCR mix (New England Biolabs) and MVM-specific primers [40]. An infectious clone of MVM was used as an external standard [48]. Amplification and real-time detection of the PCR amplicons were carried out on the CFX96 Real-Time system (Bio-Rad, USA). Logarithmic reduction values (LRVs) were calculated according to previous reports [46,47].

2.13. Infectivity titration by 50% tissue culture infectious dose (TCID50) assay

To determine the infectious MVM titer in feedstream and filtrate pools, replicates of samples were serially diluted ten-fold in PBS and added to A9 cell cultures using large volume plating to increase sensitivity [49]. Cytopathic effects were microscopically analyzed at 10 dpi and the infectious titer was calculated by the Spearman-Kärber method. The detection limit of the assay was 0.079 TCID50/mL.

3. Results and discussion

To visualize the retention of MVM as a relevant parvovirus model in the different filter membrane structures, the virus was purified from infected cell cultures and labeled before filtration with fluorescent Atto-633 dye (Supplementary Fig. 1) [40]. Furthermore, we included recombinantly expressed bacteriophage MS2 VLPs labeled with Atto-488 as a reference particle, which exhibits virtually the same capsid diameter as MVM [15]. To directly study the viral behavior inside the different membranes without the implication of other variables, such as filter fouling and flow decay, virus filtration was performed under conditions of defined low complexity, using moderate spiking doses of purified MVM-633 and MS2-488 in PBS (Supplementary Figs. 1 and 3) [39,50–52]. After filtration, the membranes were embedded into suitable polymers, cross-sectioned, and analyzed for retained viruses by LSM. To exactly localize the labeled viral particles inside the membrane structure, the filters were simultaneously scanned for autofluorescence at UV wavelengths. To obtain a comprehensive picture of the entire virus removal process, we additionally measured the viral load reduction in the filtrate by an optimized qPCR protocol [40,47] and confirmed the LRVs by TCID50 assays.

3.1. Virus retention in different filter membrane types at constant flow conditions

For decades, Planova 20N hollow fiber membranes with a nominal pore size of 19 nm have widely been used in the manufacturing of biologicals. The autofluorescence analysis of the membrane cross-sections by LSM showed a gradually increase in membrane density from the lumen of the hollow fiber to the outer edge of the filter (Fig. 1A). This transition in membrane structure conforms with previously published TEM images where the feed side had a rough texture while deeper layers towards the exit of the membrane displayed a highly dense polymer consistence concomitant with decreasing pore sizes [24,53–55].

Visualization of MVM-633 in the Planova 20N filter by LSM revealed a VRP with a maximum at 40–50% of the filter depth (Fig. 1B), which is in good agreement with previous results visualizing porcine parvovirus (PPV) [54] and parvovirus B19 (B19V) [53,55] by TEM. Conforming with the proposed multi-step retention model [21], we also observed a significant capture of viral particles in prior layers of the filter, suggesting that the thick SAL provides retentive voids at different filter depths, in which viruses are immobilized by the constraints of the convective flow. Strikingly, we also obtained an abrupt decrease of the virus retention signal in the middle of the membrane to undetectable levels as previously shown with PPV [54], suggesting a crucial change in the sieving stringency at this particular filter depth presumably due to a uniform decline of the pore sizes below the viral diameter. The exclusion of viruses from the dense exit side of the membrane implies a transition from a multi-step retention process in the first half [21] to a strict rejection mechanism according to an internal polarization model [32].

Taken together, the precise determination of the VRP of MVM-633 suggest the presence of three layers with different underlying retention properties: i) a reservoir zone, which constitutes generally larger pore sizes than the viral diameter, and thus mainly allows passage of viruses to deeper layers; ii) a parvovirus retentive layer, in which the majority of viral particles is captured within few micrometers based on mean pore sizes close to the outer capsid diameter of MVM (27–29 nm) [15]; iii) a rejection layer from which viruses are effectively excluded by pores sizes predominantly below the viral diameter (Fig. 2).

The Atto-488 labeled bacteriophage MS2 VLPs showed a predominant virus capture at a virtually identical filter depth as MVM and an overall comparable VRP. Minor differences were found in the rough layer, where less MS2-488 particles were retained in comparison to MVM, and at the front line to the rejection zone, where the bacteriophage signal declined more gradually. However, variations between differently labeled viruses should be carefully interpreted, as increased scattering effects of fluorescent dyes emitting at shorter wavelength might contribute to slightly broader signal distributions [56,57]. Using fluorescent modification of viruses excited at longer wavelength, like the Atto-633 dye, minimizes the scattering in the membrane polymer and thus provides a superior signal-to-noise ratio and a more precise localization.

In contrast to recent reports investigating particle retention in Planova 20N using high concentrations of fluorescent nanoparticles, we neither observed such a broad VRP in the first half of the membrane, nor a significant detection of particles within the rejection zone, and particularly no viral accumulation at the exit side (Fig. 1, Supplementary Fig. 4) [35,37]. These differences emphasize the importance of using the relevant virus models in order to validate the conclusions with regard to the actual risk faced in the manufacturing processes.

Analysis of the viral load reduction by qPCR showed an effective removal of virions by the Planova 20N membrane at each sampling point (LRV > 4) (Fig. 3A), similar to what has been observed in previous studies using MVM [29] and B19V [55]. Importantly, LRVs of labeled and unlabeled viruses were found to be identical in the different fractions, suggesting a negligible effect of the Atto-633 labeling on virus retention in this filter type. Finally, virus load reduction values were confirmed by TCID50 assays, measuring the infectious dose in pooled filtrate fractions (Table 1).

The Pegasus SV4 double layer filter has a homogeneous and symmetrical membrane structure as does its predecessor, the Ultipor DV20 filter (Supplementary Table 2, Supplementary Fig. 2) [19,33]. In line with this, the autofluorescence under UV light suggested a fairly uniform polymer density distribution within the two membranes (Fig. 1A and B). Notably, the filters occasionally contained small "bubbles" several micrometers in diameter, which, however, did not seem to have an

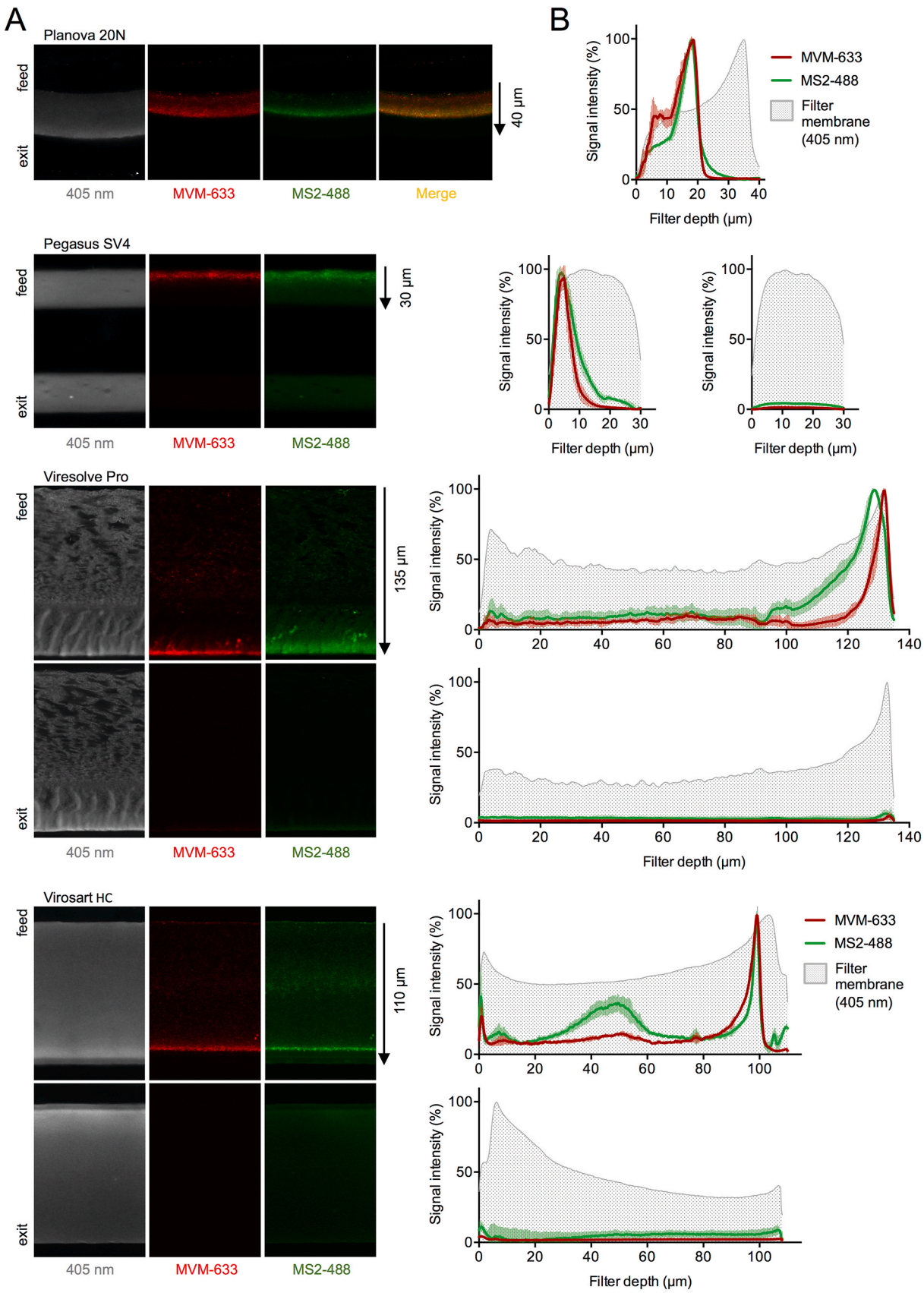

Fig. 1. Virus retention in different filter membranes under constant flow conditions. A) MVM-633 (red) and MS2-488 (green) visualized post-filtration in membrane cross-sections using laser scanning microscopy (LSM) and detection of membrane polymer autofluorescence (λ_{ex} 405 nm). B) Representation of detected signal as retention profiles, which indicate standard deviations of multiple measurements in different randomly selected membrane areas (n $\geq$ 3). (For interpretation of the references to colour in this figure legend, the reader is referred to the Web version of this article.)

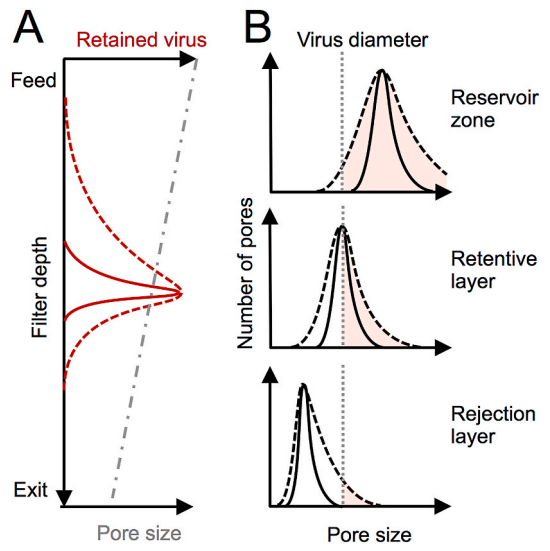

Fig. 2. Schematic depiction of expected virus retention profile in dependence to pore size distribution. A) Virus retention profiles (red) as function of the filter depth along a hypothetical pore size gradient (grey). B) Examples of narrow (solid line) or broad (dashed line) pore size distributions in the different membrane zones. Solid line in panel A shows virus retention assuming uniform pore sizes at every filter depth; dashed line indicates expected virus retention profile as consequence of a rather broad pore size distribution. The probability of virus penetration is assumed to directly correlate with the proportion of non-retentive pores in the respective membrane zones (red shaded areas in panel B). (For interpretation of the references to colour in this figure legend, the reader is referred to the Web version of this article.)

influence on the local viral capture. Retention of MVM-633 was predominately found in the first micrometers at the feed side of the filter as previously observed by 3D scanning [40], and similar to the retention pattern of fluorescent bacteriophages found in the related Ultipor DV20 filter [19,30]. Both, VRPs of MVM-633 and MS2-488 indicated a significant penetration of viruses into deeper layers of the filter, suggesting that this membrane does not constitute a strict rejection layer for viruses (Fig. 1B). This phenomenon could be explained by the combination of the shallow pore size gradient (PSG) within the uniform membrane structure and a rather broad PSD (Figs. 1 and 2, Supplementary Fig. 2) [23].

Under CF conditions, the Pegasus SV4 double layer membrane provided effective reduction of the viral load as detected by qPCR (LRV = 4.5) and TCID50 (LRV = 4.3) (Table 1). In agreement with our previous findings indicating that capsid labeling can have a minor impact on virus retention in this particular filter membrane type [40], LRVs of labeled MVM were slightly increased in comparison to the unlabeled virus (Fig. 3B). It is tempting to speculate that the non-retentive pathways in this specific membrane at CF consist of fairly uniform pore sizes marginally larger than the viral diameter. As a consequence, already small modifications of the MVM capsids (+0.33% of molecular weight, Supplementary Table 1) can significantly affect the virus retention capacity. Interestingly, however, this difference was only found in the Pegasus SV4 filter and only at CF conditions; all other filtration experiments did not reveal any detectable influence of the Atto-633 modification (Fig. 3A–D). This result reinforces previous observations that the mechanism of breakthrough may vary depending on the filter type and operating conditions [18,22,29].

The Viresolve Pro membrane represents an advancement of the

Table 1
Logarithmic reduction values (LRVs) of unlabeled MVM in pooled filtrate samples (5 × 5 mL).

	Constant flow (CF)[a]		Flow interruptions (FIs)[b]	
Filter	qPCR	TCID50	qPCR	TCID50
Planova 20N	4.4	4.8	3.1	2.5
Pegasus SV4	4.5	4.3	2.0	1.5
Viresolve Pro	≥6.5	≥6.0	5.5	4.7
Virosart HC	6.2	≥5.9	5.9	≥5.9

[a] Pressure according to the manufacturer's recommendations.
[b] Four sequential flow interruptions (30 min) every 5 mL.

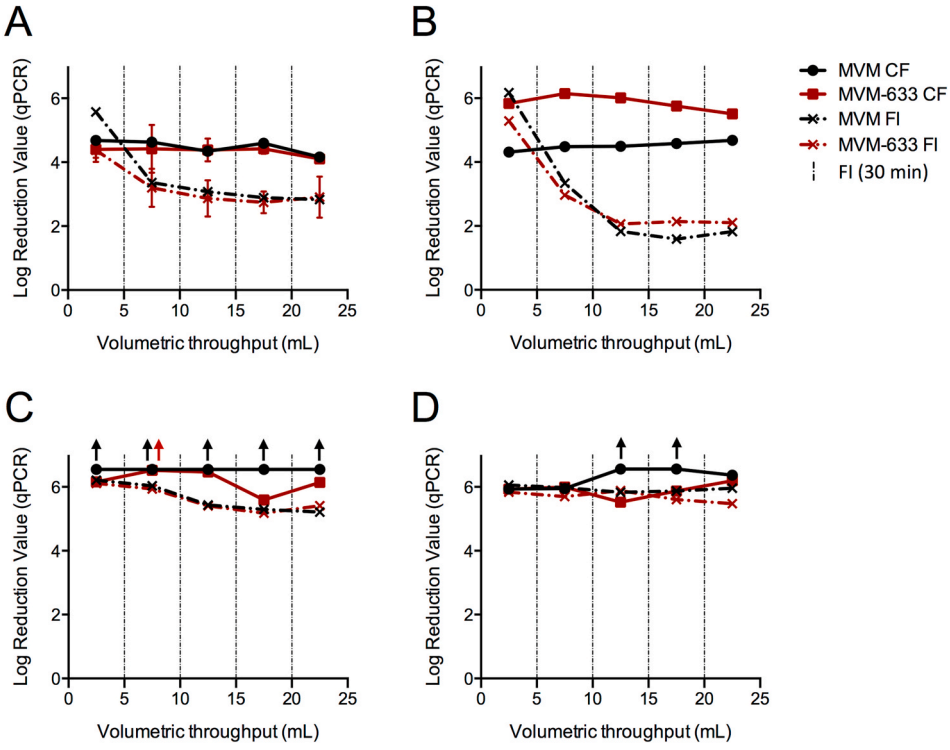

Fig. 3. Viral load reduction kinetics of unlabeled and labeled MVM in different filter membranes. Unlabeled (black) or Atto-633 labeled (red) MVM particles were filtered under constant or interrupted flow conditions using Planova 20N (A), Pegasus SV4 (B), Viresolve Pro (C) and Virosart HC (D) membranes. Logarithmic reduction values (LRVs) are based on qPCR detection of virions in nuclease-treated feed and filtrate samples [40]. Solid lines indicate filtration experiments under constant flow (CF) applying standard pressure; dashdotted lines show filtrations including four sequential flow interruptions (FIs). Arrows mark fractions where viral load was reduced to undetectable levels in the filtrate. Error bars in (A) show standard deviations of two independent filtration experiments. (For interpretation of the references to colour in this figure legend, the reader is referred to the Web version of this article.)

original Viresolve NFP filter and is commonly used for high throughput virus filtration in the downstream processing of rather pure biological products, such as monoclonal antibodies. This virus filter is composed of two membranes with a remarkably asymmetric structure, both oriented in the same direction (Supplementary Fig. 2) [33]. The thick and highly interconnected rough substrate and transition layers predominately serve as mechanical support and depth pre-filter for the thin SAL found at the exit side [24,58]. The steep PSG in the last micrometers of the membrane ends in an ultrafilter layer with a nominal pore size of 18 nm, which is conceived as effective sieving barrier for even the smallest viruses known [16,36]. The scanning of the autofluorescence illustrates this asymmetric membrane composition, showing a sharp increase of the polymer density towards the end of the filter (Fig. 1A and B). However, the imaging also revealed visible artifacts due to the mechanical cross-sectioning. Importantly, the cutting did not alter the filter depth of the retained viruses since the cross-sectioning was strictly carried out in an orthogonal direction to the filtration. The VRPs shown in Fig. 1B average the signal of a broad membrane segment and accordingly remain unaffected by the artifact-related intensity variations. Expectedly, virus retention was predominant at the end of the steep PSG of the first filter (Fig. 1), comparable to the observed capture of 20 nm gold particles in the last 5 μm [24,34]. In line with these results, electrodense stained particles were detected by TEM only a few micrometers before the exit of the first filter membrane (Supplementary Fig. 6), which can be interpreted as retained parvoviruses similar as observed in previous studies [54,55].

Interestingly, previous studies based on 3D scanning of the Viresolve Pro filter from the feed and exit side reported a significantly different retention pattern of virus models in this particular membrane [30,33,59]. PP7 and PhiX174 bacteriophages, which both have a slightly larger diameter than parvoviruses [15,25], as well as 20 nm fluorescent nanospheres were broadly retained within the entire transition zone in the last 20–30 μm of the membrane. Further studies are warranted to better understand the different results obtained using bacteriophages or artificial virus models.

Typical of a second-generation filter, the Viresolve Pro membrane provided a high retention capacity as previously described [18], reducing virions and infectivity in the filtrate to undetectable levels (LRV $\geq$6.5 and $\geq$ 5.9, respectively) (Fig. 3C, Table 1).

The Virosart HC filter is representative of the latest virus filtration technology, consisting of two rather thick membranes orientated in opposite directions. The membrane constitutes a broad SAL, which offers a high capacity to capture virus-sized particles, including fouling aggregates [24,27]. Fig. 1 provides the first visualization of viral particles inside this type of membrane, showing that both MVM-633 und MS2-488 were retained at a very distinct filter depth in the last third of the first membrane and a few micrometers before the maximal filter density. This localization of the viruses correlates well with the PSG determined by differently sized gold nanoparticles [24]. The remarkably sharp retention peak of MVM-633 within the shallow gradient confirms the monodispersity of the parvovirus spike material (Supplementary Fig. 1), as well as exemplifies the uniform transition to smaller pore sizes in this particular filter. Moreover, the abrupt decline of the front line signal towards the exit suggests an effective rejection of viral particles by the densest membrane region.

The virus load reduction measurements expectedly resulted in robust clearance of MVM in this second-generation filter type, consistently demonstrating LRVs $\geq$5.5 for both qPCR and TCID50 assays (Fig. 3D, Table 1). Previous studies reported similar or even higher reduction values using different parvovirus and bacteriophage models, explaining the robust viral retention by a narrow PSD in the SAL [11,23–25,27].

In summary, to exactly localize the fluorescently labeled viruses within the different filter structures, the membrane preparation and detection by LSM was further optimized [40]. The high-resolution scans of the cross-sections revealed that the uniformly sized viruses were retained in a characteristic profile and at a well-defined depth in the SALs of the different filters [24]. In all membranes, we consistently found that predominant parvovirus retention occurred $\leq$20 μm prior to the maximum density of membrane autofluorescence (Fig. 1A and B), which likely illustrates the consensus in the individual approaches of the different manufacturers to achieve an economical filtration process, i.e. finding the balance between effective virus retention, maximal product transmission, high filter fouling capacity, and low hydraulic resistance to increase the throughput. The remaining variations in the rejection zone morphology and thickness reflect how each filter design prioritizes the different features. For instance, the ultrafilter-like Viresolve Pro membrane, which has the steepest PSG and is known for high throughput but rather low fouling capacity, expectedly showed the shortest distance between the virus retention peak and the filter density maximum [24]. In contrast, MVM-633 was effectively captured already relatively distant from the highest density in the Planova 20N filter; the hollow fiber membrane needs to possess its entire retention capacity in one single layer and is believed to retain viruses by a fairly fouling-resistant multistep-retention mechanism using a shallow PSG [21,39]. With regard to previously published data, it is tempting to speculate that the detected viral retention peak width is a direct consequence of the PSD within the SAL (Fig. 2) [23,27]. Accordingly, a narrow VRP indicates a higher selectivity in the separation-active zone, which favors both a robust virus retention and high recovery of the therapeutic protein.

From a holistic view, the retention patterns of MVM-633 virtually superpose with the VRPs of MS2-488, whose particles have a very similar outer capsid diameter compared to MVM [15], but minor differences in the surface charge and hydrophobicity properties [40,60,61]. This result demonstrates that the virus retention in the tested filter types is predominantly determined by size-exclusion (Fig. 1). Nevertheless, examination of the VRPs in more detail revealed notable differences between these unrelated viruses. In Pegasus SV4 and Virosart HC filters, MS2-488 showed a slightly deeper migration compared to MVM-633, while the inverse was observed for the Viresolve Pro membrane. Moreover, although the retention profile of MVM and MS2 was very similar close the rejection zone, it appeared rather different in layers with larger pore sizes, suggesting certain virus-specific retention mechanisms depending on the filter type. This phenomenon cannot be attributed to a different virus preparation, as some of these experiments were simultaneously performed using the same spike material. The slightly different retention profiles of these two viruses might be explained by a different adsorption to the characteristic filter membrane materials (Supplementary Table 2).

Taken together, the detection of Atto-633 labeled MVM in membrane cross-sections by LSM allowed an accurate localization of the retained parvoviruses within the porous polymer networks, providing direct insights into the structure-function relationship of the four analyzed filters.

3.2. *Virus retention in early filter generations after repeated flow interruptions*

In virus filtration of biotherapeutics, the pressure may be released to change product intermediate bags, to include buffer flushes at the end of processes, or as a consequence of unplanned process stops [18]. However, FIs can cause substantial reduction of the LRV depending on the filter type, product matrix [29], and pressure release duration [22]. To investigate the effects of FIs on virus retention and breakthrough in the different membranes, the following series of virus filtration experiments included four repeated pressure releases of 30 min each, which is sufficient time for entrapped viruses to diffuse into potentially accessible non-retentive pores [22].

In filtration experiments using the Planova 20N membrane, LRV kinetics measured by qPCR showed a moderate but significant breakthrough of virions to the permeate, reaching a steady state of 3 log10 virus reduction after two pressure releases (Fig. 3A, Table 1). These

results corroborate observations of the filter manufacturer, reporting similar LRVs under low flow conditions or after FIs [29]. The mathematical model and experimental results of Yamamoto et al. suggest that virus retention in this filter type is primarily dependent on the maximal pore size, which becomes particularly evident during low or no flow conditions when the retention capacity is already reduced [21]. The obtained LRV steady state after two FIs has been explained by the saturation of the available non-retentive pathways in the filter membrane [26].

To directly compare VRPs relative to the filter structure in different experiments, signals of the membrane autofluorescence were normalized and superposed to colocalize the feed and exit side, and characteristic hallmarks in the filter density profile (Supplementary Fig. 7). The comparison of the VRPs in the Planova 20N membrane revealed i) a decreased proportion of both MVM and MS2 VLPs in the reservoir zone, and ii) a significant compression and shift of the retention peak into deeper membrane layers of the retentive zone (Fig. 4A–C). Similar to CF conditions, the fluorescent signal was still found to rapidly decline towards the densest region of the cross-section, suggesting a still continued effective size-based exclusion of the viruses at the interface to the rejection layer (Supplementary Fig. 4B). The results confirm that interruption of the convective flow leads to a diffusion-based mobilization of viral particles from retentive voids in the reservoir zone as previously simulated [21]. When filter flow was restarted, mobilized viruses likely re-challenged the rejection zone, which caused a slightly deeper migration into more dense membrane layers. Similarly, at operating conditions below the recommended low pressure limit [29], a recent study observed a time-dependent shift of the MVM VLP retention peak towards the exit of the Planova 20N membrane [62].

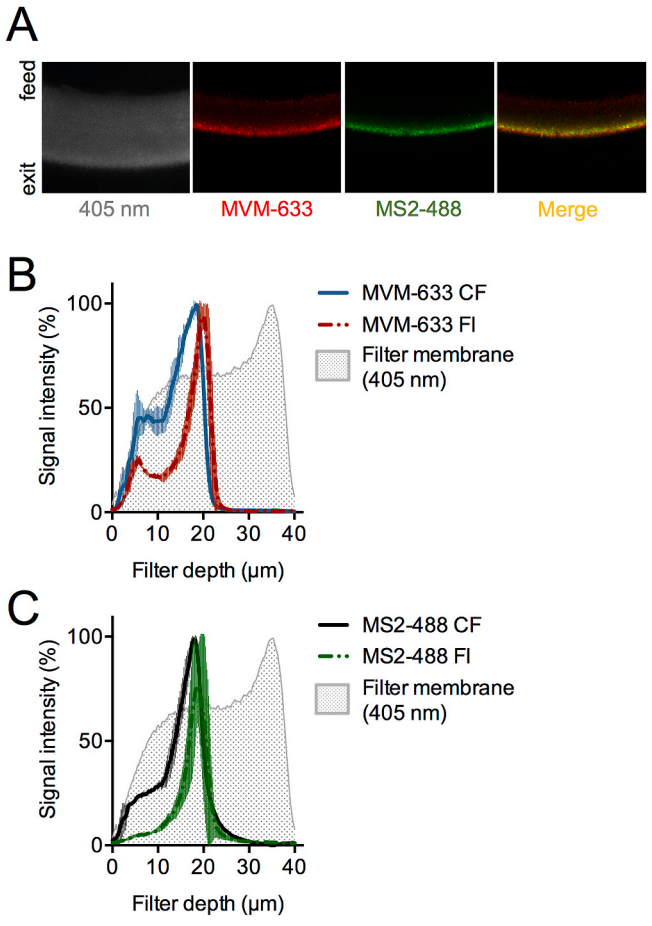

Fig. 4. Virus retention in the Planova 20N hollow fiber membrane after repeated flow interruptions (FIs). A) Membrane cross-sections analyzed by laser scanning microscopy, showing polymer autofluorescence (λ_{ex} 405 nm) and retention patterns of retained fluorescent MVM-633 and MS2-488. Virus retention profiles (VRPs) of MVM-633 (B) and MS2-488 (C) after FIs are superposed onto VRPs obtained after constant flow (CF) conditions (Fig. 1). Error bars indicate standard deviations of multiple measurements in different membrane areas ($n \geq 3$).

To increase the robustness of Planova 20N filtration, manufacturers of biotherapeutics occasionally implement two consecutive filter units (serial filtration), thus mimicking the concept of a double layer membrane. Notably, the advanced Planova BioEX hollow-fiber membranes provide robust virus removal even after repeated process interruptions [29].

In virus filtrations using the Pegasus SV4 membrane, repeated pressure releases considerably compromised the virus reduction capacity of the filter (Fig. 3B). The LRVs of the fractions rapidly decreased upon FIs and reached a low steady state (LRV = 2) after two stops. The high breakthrough of viruses was confirmed by the infectivity assays (Table 1) and is in accordance with previous results obtained under low flow conditions [26]. In contrast, the Pegasus Prime next generation filter, from the same manufacturer, showed more robust virus clearance under comparable process conditions [26].

In filtration experiments using the Ultipor DV20 membrane, which is considered a predecessor of the Pegasus SV4, FIs caused substantial temporary drops in virus reduction [19,59], which was associated with the migration of fluorescently labeled bacteriophages to deeper membrane layers. Indeed, detection of MVM-633 by LSM indicated an apparent broadening of the retained signal at the entry of the Pegasus SV4 filter, and in some cases, visible penetration of the virus even to the exit side of the first layer (Fig. 5A and B). The most striking effect, however, was the visible breakthrough to the second membrane layer. While most of the analyzed second layer cross-sections only showed minor or barely detectable signal, several regions indicated remarkable local accumulations of viruses (Fig. 5A). Due to this uneven signal distribution in the second membrane, VRPs after FIs showed remarkable variabilities (Fig. 5C).

To further characterize this breakthrough phenomenon and to exclude a technical artifact, the entire filter depth of an intact double layer membrane segment was scanned (Fig. 5D, Supplementary Fig. 5). The 3D reconstruction of the stacks confirmed local breakthrough foci of viruses on the second layer. The view from the feed side onto the combined or single stacks of the first membrane revealed no microscopically visible differences in the membrane density or mechanical damage (Fig. 5E, Supplementary Fig. 9). Furthermore, no correlation was found between the occurrence of the previously described 'bubbles' and the breakthrough foci on the second membrane.

The diffusion-based model proposes that viruses drift during FIs and may access non-retentive pathways through the membrane layer after the convective flow is restarted [21,27]. Accordingly, viruses found in breakthrough foci on the second layer should originate from regions of the first membrane layer lying immediately above these accumulations [58], and these particular regions should exhibit a slightly lower retention signal. Indeed, we observed a certain tendency conforming to this expectation; however, slightly lower signal was also detected in other regions of the first membrane layer that did not correlate with a visible breakthrough to the underlying area of the second layer. Also, the analysis of the single stacks did not reveal any conspicuous irregularities to explain this local virus passage (Supplementary Fig. 9).

To gain a more comprehensive view of the foci-related breakthrough phenomenon, the signal of randomly selected membrane regions with as larger surface area (1 mm^2) were analyzed (Fig. 6A–C). The combined stacks were examined with the ImageJ program, quantifying individual pixel intensities and calculating overall and local signal distributions (Supplementary Fig. 10A). The relative quantification of the virus signal between different layers and flow conditions demonstrates an increased breakthrough of viruses to the second membrane layer after FI in comparison to CF conditions (Fig. 6D). Furthermore, the irregular

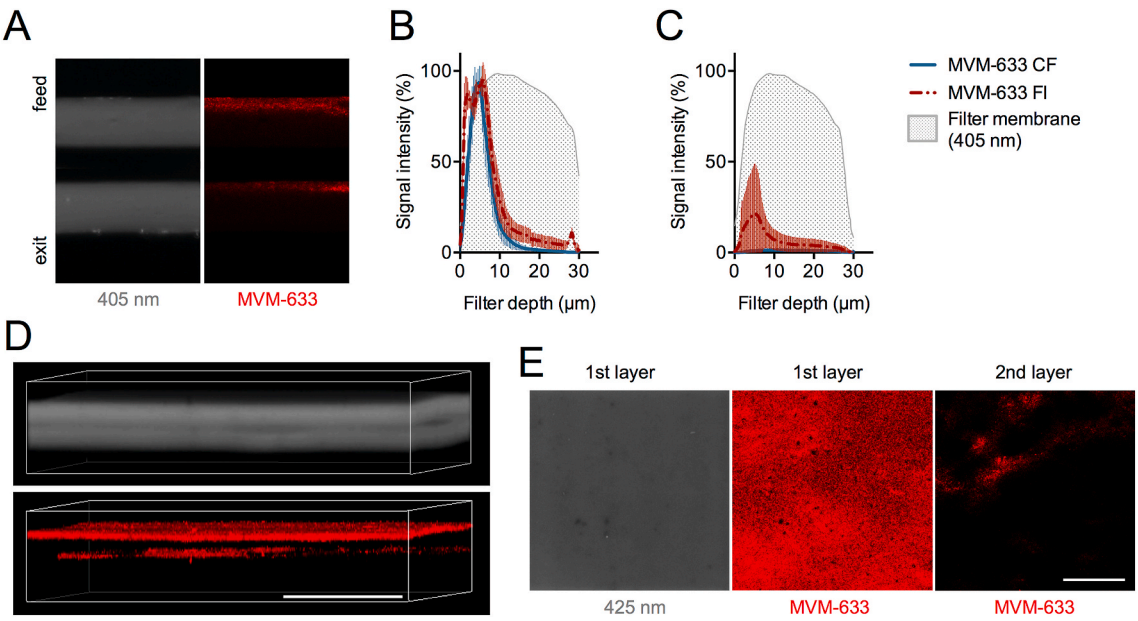

Fig. 5. Virus retention in the Pegasus SV4 double filter membrane after repeated flow interruptions (FIs). A) Selected membrane cross-section analyzed by laser scanning microscopy, showing polymer autofluorescence (λ_{ex} 405 nm) and retention pattern of retained fluorescent MVM-633. Virus retention profiles (VRPs) of MVM-633 in first (B) and second (C) membrane layer after FIs are superposed onto VRPs obtained after constant flow (CF) conditions (Fig. 1). Error bars indicate standard deviations of multiple measurements in different membrane areas ($n \geq 3$). D) 3D scanning of intact double layer membrane after repeated FIs, showing autofluorescence (λ_{ex} 425 nm) and MVM-633 retention. E) Analysis of combined stackes visualized from the top. Scale bar in D) and E) = 100 µm.

distribution of the virus penetration to the second layer suggest significant differences of the local retention capacities in different membrane areas (Fig. 6C and D, Supplementary Figs. 10B–D).

To better characterize this locally restricted penetration of viruses, we visually identified and marked foci on the second membrane layer and individually analyzed these areas with the image software (Supplementary Fig. 11). Across the 10 mm^2, we found in total 163 foci, corresponding to an average of 16.3 foci/mm^2. However, the number of foci per segment was highly variable, ranging from 0 to 35 foci/mm^2 (Fig. 6E). Together, the identified foci combined for 83.2% of the total signal found on the second membrane layer, i.e. that only 16.8% of the breakthrough signal was not found associated to locally enhanced transmission (Table 2). Half of the viral breakthrough was found to be attributed to only 24 major foci, and further 25% breakthrough to 58 intermediate foci (Fig. 6F, Table 2), which underlines that the majority of the viruses break through a few locally restricted low-retentive areas.

To examine the heterogeneity of the foci population, the breakthrough signal of each focus was plotted as a function of the membrane area affected. The correlation reveals that both the distribution and the appearance of the foci are diverse (Fig. 6G). The plot shows on one hand relatively large foci with a rather low average breakthrough signal, and on the other hand remarkably concentrated signal on relatively small surfaces. Breakthrough foci with an average pixel intensity of more than 0.1 RFU represent local membrane regions, which provide less than 1 log10 virus-reduction capacity (Fig. 6G). Superposition of such low-retentive areas in the double-layer membrane arguably cause practically unhindered local viral breakthrough to the permeate, which explains the exceptionally low LRV of this filter type after FIs.

The commonly accepted mathematical simulations predict the virus retention capacity of a filter membrane based on the ratio between retentive and non-retentive pores [21,23]. The model relies on an average PSD, assuming uniform composition of the entire filter membrane. However, the visual and quantitative analyses of the Pegasus SV4 filter after FIs demonstrate that the passage of viruses through the membrane layers predominately occurs through local clusters of breakthrough foci. The accumulation of non-retentive pathways suggests crucial local variations in the PSD in this particular membrane and possibly also in other filters. Complementing the model with local pore size variabilities may provide more accurate simulations for the viral breakthrough in the different membrane types.

3.3. *Virus retention in second filter generation after repeated flow interruptions*

Virus filtration experiments using Viresolve Pro filters consistently resulted in an effective removal of MVM and only a minor LRV decay even after repeated FIs (LRV $\geq$ 4.7) (Fig. 3C, Table 1). This observation conforms with the virus reduction capacity measured under constant and interrupted flow conditions in previous studies [18,59].

The comparisons of the MVM-633 retention profiles elucidated that FIs lead to an enhanced accumulation of the virus in close proximity to the exit side of the first Viresolve Pro membrane (Fig. 7A and B), and virtually no detectable signal in the rest of the filter. This finding suggests that the entrapped viruses in the substrate and transition layer during CF were released and subsequently migrated deeper after the FIs until being rejected by the ultrafilter layer at the very end of the filter. The diffusion-based mobilization from the retentive voids in the rougher layers and lateral movement to non-retentive pores might be additionally facilitated by the high void interconnectivity of this filter type [58]. The migration and accumulation of MVM capsids at the final sieving barrier stands in sharp contrast to the previously proposed capture mechanism in the transition zone observed with PhiX174 bacteriophages [59]. This different result again emphasizes the importance of verifying conclusions regarding virus retention mechanisms with parvoviruses as representative models, using highly purified and monodisperse spike material.

Virus filtration experiments using Virosart HC filter membranes consistently showed a robust removal of MVM even after repeated pressure releases (LRV $\geq$ 5.9) (Fig. 3D, Table 1) as previously reported with bacteriophages [27]. In line with this effective reduction, MVM-633 retention profiles after CF and FIs virtually superposed in all filter depths (Fig. 8A and B). The detailed analysis indicated only a minor broadening of the signal in the SAL and possibly a slightly deeper retention of the front line. In sum, the visualization of the virus inside

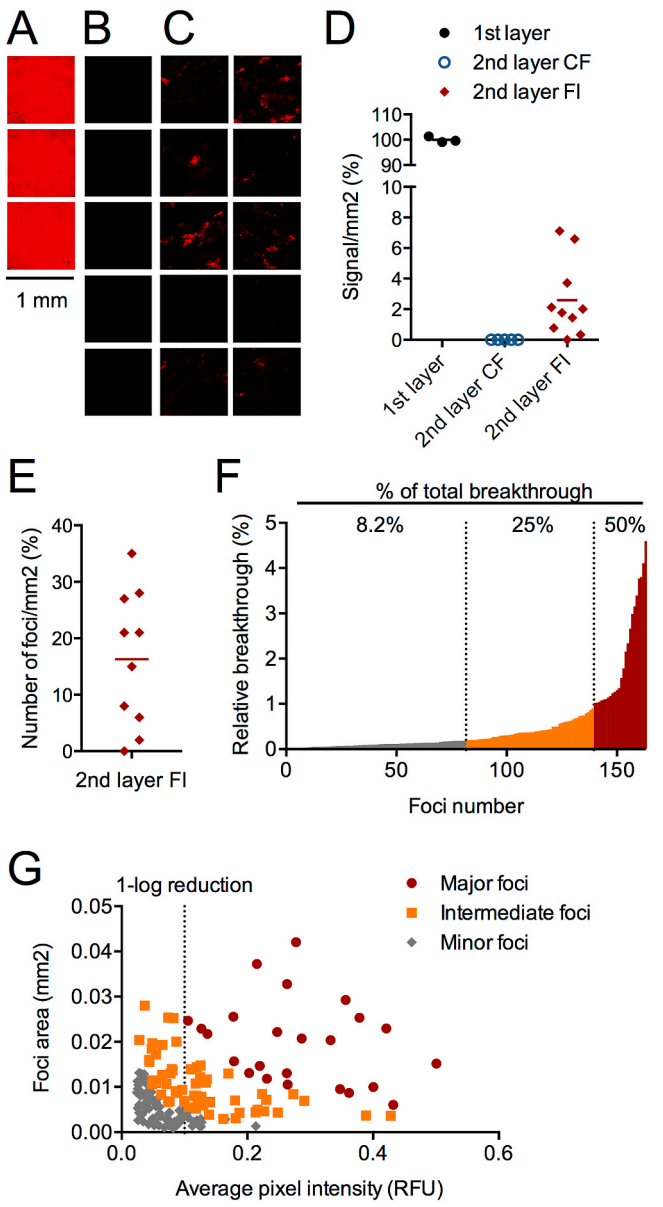

Fig. 6. Quantitative analysis of Pegasus SV4 membrane layers after filtration at constant flow (CF) or interrupted flow (FI). Laser scanning microscopy images of randomly selected membrane areas show retention of MVM-633 in (A) first layer, (B) second layer after CF, and (C) second layer after FI. D) Total signal detected in analyzed membrane areas, normalized to average signal/mm^2 on first membrane. E) Variation in number of foci/mm2 on second membrane layer segments after FIs. F) Identified 163 foci on 10 mm^2 ordered according to their relative breakthrough. Foci are categorized as major foci (combine for 50% of total breakthrough), intermediate foci (25%), and minor foci (8.2%). G) Scatter plot of breakthrough foci as function of their area and average pixel intensity. Dotted line marks threshold of 1-log reduction in comparison to detected virus retention on first layer. RFU, relative fluorescence units.

the Virosart HC membrane suggests an effective entrapment of the virus and a strict rejection of viral particles by the densest membrane layers, which can be explained by the reported narrow PSD in this filter [23,24,27]. The limited number of non-retentive pores apparently prevents potential mobilization of viruses, lateral diffusion during FIs, and deeper migration of viruses after restarting the flow.

In agreement with previous reports, our results confirm a significantly different performance of the four filter types after repeated pressure releases [18,22,59]. While both second-generation filters Viresolve Pro and Virosart HC, provided effective and robust virus removal under the different flow conditions, the earlier generation filters exhibited a higher breakthrough of viruses after FIs (Fig. 3, Table 1). Conforming with the diffusion-based model, we found a visible mobilization of viruses from retentive voids in the reservoir zone, and subsequent migration into deeper layers particularly in the filters that showed a negative impact on LRVs by FIs (Figs. 3–5). In the asymmetric Planova 20N and Viresolve Pro membranes, deeper migrating viral particles after FIs were stopped by the rejection layer according to a strict internal polarization model (Figs. 2, 4 and 7) [32]. Although the accumulation and increased challenge of the rejection layer caused a detectable decrease of the retention capacity as previously predicted (Fig. 3, Table 1) [19], the strict exclusion from the densest membrane zone appeared to provide an effective barrier to withstand even repeated pressure releases, allowing only a moderate increase in virus breakthrough. In contrast, the rather symmetric structure of the Pegasus SV4, which did not indicate a clear rejection layer, showed significant virus penetration under the regime of serial FIs (Fig. 5). A generally narrow PSD along the entire PSG as found in the new-generation filter membranes (e.g. Virosart HC) [23–25,27], seems to favor both, a selective capture and immobilization of the virus within a narrow retentive layer, as well as a strict exclusion of viral particles by the rejection zone (Figs. 2 and 8). This example illustrates how the filter manufacturers successfully developed more robust membranes by assuring a narrow PSD in the SAL, thus reducing the number of larger pores and minimizing the probability that viruses can access non-retentive pathways when the constraints of the convective flow are absent [21,23,25,27].

Previous results have shown that low and no flow conditions exerts comparable effects on the virus reduction capacity, as both conditions increase the Brownian motion of the viral particles inside the retentive voids. Accordingly, our findings not only represent the specifically studied pressure release events, but are expected to similarly apply to other process conditions where the filtration flow has declined.

However, in contrast to the defined conditions used in this work, feedstreams in the manufacturing of biotherapeutic products are far more complex and may cause filter fouling and potential interactions with viruses [27]. Several studies emphasize that the virus reduction capacity is substantially influenced by product-specific compositions, which may enhance or decrease robustness of virus retention, and accordingly, the process development and validation need to be done on a case-by-case basis [18,29]. Therefore, to gain deeper insights into the underlying mechanisms, future studies are warranted to visualize parvoviruses inside the membrane under manufacturing conditions.

Table 2
Breakthrough foci categories identified on 10 mm^2 of second membrane layer of Pegasus SV4 filter after repeated flow interruptions.

Foci category	Combined breakthrough (%)	Number of foci	Average signal intensity (RFU)[a]	Average area (mm^2)	Combined area (%)
Major	50.1	24	0.280	0.020	4.8
Intermediate	24.9	58	0.129	0.011	6.2
Minor	8.2	81	0.064	0.005	4.2
Not assigned[b]	16.8	n.a.	0.005	n.a.	84.8

[a] Relative fluorescence unit (RFU) of 1 corresponds to retained signal found on first membrane layer.
[b] Areas of filter membrane where no visual accumulation of breakthrough signal was identified (Supplementary Fig. 11).

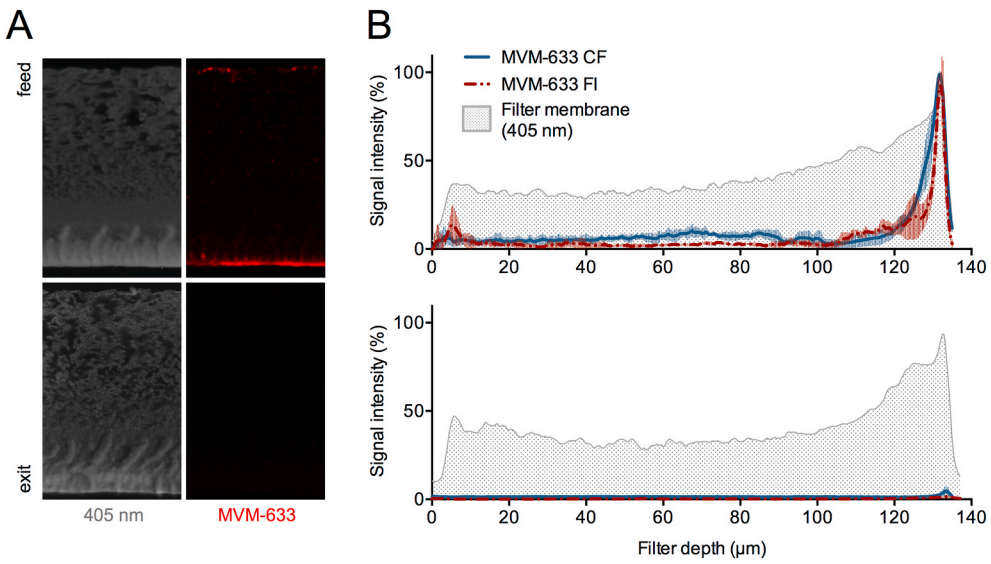

Fig. 7. Virus retention in the Viresolve Pro double filter membrane after repeated flow interruptions (FIs). A) Representative membrane cross-sections analyzed by laser scanning microscopy, showing polymer autofluorescence (λ_{ex} 405 nm) and retention pattern of retained fluorescent MVM-633. B) Virus retention profiles (VRPs) of MVM-633 in first and second membrane layer after FIs are superposed onto VRPs obtained after constant flow (CF) conditions (Fig. 1).

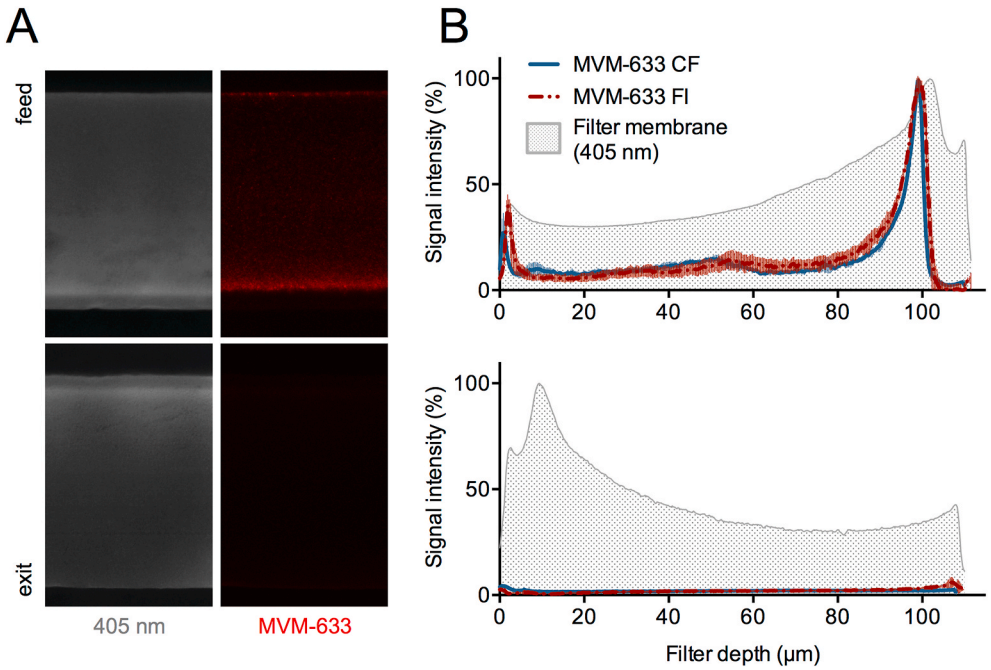

Fig. 8. Virus retention in the Virosart HC double filter membrane after repeated flow interruptions (FIs). A) Representative membrane cross-sections analyzed by laser scanning microscopy, showing polymer autofluorescence (λ_{ex} 405 nm) and retention pattern of retained fluorescent MVM-633. B) Virus retention profiles (VRPs) of MVM-633 in first and second membrane layer after FIs are superposed onto VRPs obtained after constant flow (CF) conditions (Fig. 1).

4. Conclusion

The retention of viral particles in virus filter membranes is known to be predominately determined by a size-based exclusion mechanism. However, it remained unclear where exactly in the porous structure of the membranes the relevant parvoviruses are captured and how certain operating conditions, such as FIs, influence the virus retention inside the intricate membrane network. Here, we identified the parvovirus retentive layers in four commercially available nanofilters. The visualization of the filter-specific VRPs provided novel information about the structure-function relationships of the different membrane designs. FIs lead to visible mobilization of viruses in the reservoir zone and a deeper migration of viral particles into denser polymer layers particularly in the first-generation filters, where pressure releases compromised the virus reduction capacity. Moreover, in the most affected filter, we discovered the phenomenon of breakthrough foci, where significant penetration of viruses through the membrane occurred on locally restricted areas.

Taken together, the mechanistic insights into the flow-dependent retention of MVM inside different nanofilter structures generally confirmed the previously described influences of the hydrodynamic force on the virus entrapment in the porous membrane network. However, the visualization of this relevant parvovirus also revealed novel phenomena, like the breakthrough foci, and qualified previous assertions obtained based on artificial virus models. A deeper understanding

of the underlying retention and breakthrough mechanisms will help to specifically optimize filter membranes and design spaces in order to increase the performance and safety margin in industrial virus filtration processes.

CRediT authorship contribution statement

Remo Leisi: Conceptualization, Methodology, Investigation, Formal analysis, Writing – original draft, Writing - review & editing. **Eleonora Widmer:** Conceptualization, Funding acquisition, Writing - review & editing. **Barry Gooch:** Writing - review & editing. **Nathan J. Roth:** Conceptualization, Funding acquisition, Writing - review & editing, Supervision. **Carlos Ros:** Conceptualization, Funding acquisition, Writing - review & editing, Supervision, Project administration.

Declaration of competing interest

The authors declare that they have no known competing financial interests or personal relationships that could have appeared to influence the work reported in this paper.

Acknowledgment

We would like to acknowledge the University of Bern and CSL Behring AG for their support of this work. We also thank Beat Hänni and Marianne Hofstetter from the Institute of Anatomy at the University of Bern for their assistance with membrane cross-sectioning and EM. EM sample preparation and imaging were performed with devices supported by the Microscopy Imaging Center (MIC) of the University of Bern.

Appendix A. Supplementary data

Supplementary data to this article can be found online at https://doi.org/10.1016/j.memsci.2021.119548.

References

[1] M.M. Lieber, R.E. Benveniste, D.M. Livingston, G.J. Todaro, Mammalian cells in culture frequently release type C viruses, Science 182 (80) (1973) 56–59, https://doi.org/10.1126/science.182.4107.56.
[2] R.L. Garnick, Raw materials as a source of contamination in large-scale cell culture, Dev. Biol. Stand. 93 (1998) 21–29.
[3] M. Moody, W. Alves, J. Varghese, F. Khan, Mouse minute virus (MMV) contamination - a case study: detection, root cause determination, and corrective actions, PDA J. Pharm. Sci. Technol. (2011) 580–588, https://doi.org/10.5731/pdajpst.2011.00824.
[4] P.W. Barone, M.E. Wiebe, J.C. Leung, I.T.M. Hussein, F.J. Keumurian, J. Bouressa, A. Brussel, D. Chen, M. Chong, H. Dehghani, L. Gerentes, J. Gilbert, D. Gold, R. Kiss, T.R. Kreil, R. Labatut, Y. Li, J. Müllberg, L. Mallet, C. Menzel, M. Moody, S. Monpoeho, M. Murphy, M. Plavsic, N.J. Roth, D. Roush, M. Ruffing, R. Schicho, R. Snyder, D. Stark, C. Zhang, J. Wolfrum, A.J. Sinskey, S.L. Springs, Viral contamination in biologic manufacture and implications for emerging therapies, Nat. Biotechnol. (2020), https://doi.org/10.1038/s41587-020-0507-2.
[5] N.J. Roth, Pathogen reduction of blood components and plasma derivatives, in: Ross. Princ. Transfus. Med., 2016, pp. 632–641. https://doi.org/10.1002/9781119013020.ch56.
[6] EMA/CHMP/BWP/706271/2010, Guideline on plasma-derived medicinal products, 2011.
[7] R. Cameron, K. Smith, Virus clearance methods applied in bioprocessing operations: an overview of selected inactivation and removal methods, Pharm. Bioprocess. 2 (2014) 75–83, https://doi.org/10.4155/pbp.13.61.
[8] S. Caballero, J.M. Diez, F.J. Belda, M. Otegui, S. Herring, N.J. Roth, D. Lee, R. Gajardo, J.I. Jorquera, Robustness of nanofiltration for increasing the viral safety margin of biological products, Biologicals 42 (2014) 79–85, https://doi.org/10.1016/j.biologicals.2013.10.003.
[9] N.J. Roth, H.O. Dichtelmüller, F. Fabbrizzi, E. Flechsig, A. Gröner, M. Gustafson, J. I. Jorquera, T.R. Kreil, D. Misztela, E. Moretti, M. Moscardini, G. Poelsler, J. More, P. Roberts, A. Wieser, R. Gajardo, Nanofiltration as a robust method contributing to viral safety of plasma-derived therapeutics: 20 years' experience of the plasma protein manufacturers, Transfusion 60 (2020) 2661–2674, https://doi.org/10.1111/trf.16022.
[10] E. Gefroh, H. Dehghani, M. McClure, L. Connell-Crowley, G. Vedantham, Use of MMV as a single worst-case model virus in viral filter validation studies, PDA J. Pharm. Sci. Technol. 68 (2014) 297–311, https://doi.org/10.5731/pdajpst.2014.00978.
[11] T. Nowak, B. Popp, N.J. Roth, Choice of parvovirus model for validation studies influences the interpretation of the effectiveness of a virus filtration step, Biologicals 60 (2019) 85–92, https://doi.org/10.1016/j.biologicals.2019.04.003.
[12] A.L. Llamas-Saiz, M. Agbandje-McKenna, W.R. Wikoff, J. Bratton, P. Tattersall, M. G. Rossmann, Structure determination of minute virus of mice, Acta Crystallogr. Sect. D Biol. Crystallogr. 53 (1997) 93–102, https://doi.org/10.1107/S0907444996010566.
[13] L. Govindasamy, K. Hueffer, C.R. Parrish, M. Agbandje-McKenna, Structures of host range-controlling regions of the capsids of canine and feline parvoviruses and mutants, J. Virol. 77 (2003) 12211–12221, https://doi.org/10.1128/jvi.77.22.12211-12221.2003.
[14] B. Kaufmann, A.A. Simpson, M.G. Rossmann, The structure of human parvovirus B19, Proc. Natl. Acad. Sci. U.S.A. 101 (2004) 11628–22633, https://doi.org/10.1073/pnas.0402992101.
[15] V.S. Reddy, P. Natarajan, B. Okerberg, K. Li, K.V. Damodaran, R.T. Morton, C. L. Brooks, J.E. Johnson, Virus particle explorer (VIPER), a website for virus capsid structures and their computational analyses, J. Virol. 75 (2001) 11943–11947, https://doi.org/10.1128/jvi.75.24.11943-11947.2001.
[16] G. Bolton, M. Cabatingan, M. Rubino, S. Lute, K. Brorson, M. Bailey, Normal-flow virus filtration: detection and assessment of the endpoint in bioprocessing, Biotechnol. Appl. Biochem. 42 (2005) 133, https://doi.org/10.1042/ba20050056.
[17] M. Asper, Virus breakthrough after pressure release during virus retentive filtration, in: Parenter. Drug Assoc. Virus TSE Saf. Forum, Barcelona, Spain, 2011.
[18] D. LaCasse, P. Genest, K. Pizzelli, P. Greenhalgh, L. Mullin, A. Slocum, Impact of process interruption on virus retention of small-virus filters, Bioprocess Int 11 (2013) 34–44.
[19] M.A. Woods, A.L. Zydney, Effects of a pressure release on virus retention with the Ultipor DV20 membrane, Biotechnol. Bioeng. 111 (2014) 545–551, https://doi.org/10.1002/bit.25112.
[20] R. Fan, F. Namila, D. Sansongko, S.R. Wickramasinghe, M. Jin, D. Kanani, X. Qian, The effects of flux on the clearance of minute virus of mice during constant flux virus filtration, Biotechnol. Bioeng. (2021), https://doi.org/10.1002/bit.27778.
[21] A. Yamamoto, T. Hongo-Hirasaki, Y. Uchi, H. Hayashida, F. Nagoya, Effect of hydrodynamic forces on virus removal capability of Planova™ filters, AIChE J. 60 (2014) 2286–2297, https://doi.org/10.1002/aic.14392.
[22] D. LaCasse, S. Lute, M. Fiadeiro, J. Basha, M. Stork, K. Brorson, R. Godavarti, C. Gallo, Mechanistic failure mode investigation and resolution of parvovirus retentive filters, Biotechnol. Prog. 32 (2016) 959–970, https://doi.org/10.1002/btpr.2298.
[23] P. Kosiol, B. Hansmann, M. Ulbricht, V. Thom, Determination of pore size distributions of virus filtration membranes using gold nanoparticles and their correlation with virus retention, J. Membr. Sci. 533 (2017) 289–301, https://doi.org/10.1016/j.memsci.2017.03.043.
[24] P. Kosiol, M.T. Müller, B. Schneider, B. Hansmann, V. Thom, M. Ulbricht, Determination of pore size gradients of virus filtration membranes using gold nanoparticles and their relation to fouling with protein containing feed streams, J. Membr. Sci. 548 (2018) 598–608, https://doi.org/10.1016/j.memsci.2017.11.048.
[25] S. Giglia, D. Bohonak, P. Greenhalgh, A. Leahy, Measurement of pore size distribution and prediction of membrane filter virus retention using liquid-liquid porometry, J. Membr. Sci. 476 (2015) 399–409, https://doi.org/10.1016/j.memsci.2014.11.053.
[26] L. David, J. Niklas, B. Budde, M. Lobedann, G. Schembecker, Continuous viral filtration for the production of monoclonal antibodies, Chem. Eng. Res. Des. 152 (2019) 336–347, https://doi.org/10.1016/j.cherd.2019.09.040.
[27] P. Kosiol, C. Kahrs, V. Thom, M. Ulbricht, B. Hansmann, Investigation of virus retention by size exclusion membranes under different flow regimes, Biotechnol. Prog. 35 (2019), https://doi.org/10.1002/btpr.2747.
[28] A. Wieser, A. Berting, C. Medek, G. Poelsler, T.R. Kreil, Virus filtration and flow variation: an approach to evaluate any potential impact on virus retention, PDA J. Pharm. Sci. Technol. 70 (2016) 325–331, https://doi.org/10.5731/pdajpst.2015.006346.
[29] D. Strauss, J. Goldstein, T. Hongo-Hirasaki, Y. Yokoyama, N. Hirotomi, T. Miyabayashi, D. Vacante, Characterizing the impact of pressure on virus filtration processes and establishing design spaces to ensure effective parvovirus removal, Biotechnol. Prog. 33 (2017) 1294–1302, https://doi.org/10.1002/btpr.2506.
[30] M. Bakhshayeshi, N. Jackson, R. Kuriyel, A. Mehta, R. van Reis, A.L. Zydney, Use of confocal scanning laser microscopy to study virus retention during virus filtration, J. Membr. Sci. 379 (2011) 260–267, https://doi.org/10.1016/j.memsci.2011.05.069.
[31] M. Inouye, T. Burnouf, The role of nanofiltration in the pathogen safety of biologicals: an update, Curr. Nanosci. 16 (2019) 413–424, https://doi.org/10.2174/1573413715666190328223130.
[32] N.B. Jackson, M. Bakhshayeshi, A.L. Zydney, A. Mehta, R. van Reis, R. Kuriyel, Internal virus polarization model for virus retention by the Ultipor® VF Grade DV20 membrane, Biotechnol. Prog. 30 (2014) 856–863, https://doi.org/10.1002/btpr.1897.
[33] F. Fallahianbijan, S. Giglia, C. Carbrello, A.L. Zydney, Use of fluorescently-labeled nanoparticles to study pore morphology and virus capture in virus filtration membranes, J. Membr. Sci. 536 (2017) 52–58, https://doi.org/10.1016/j.memsci.2017.04.066.
[34] H. Nazem-Bokaee, F. Fallahianbijan, D. Chen, S.M. O'Donnell, C. Carbrello, S. Giglia, D. Bell, A.L. Zydney, Probing pore structure of virus filters using scanning

electron microscopy with gold nanoparticles, J. Membr. Sci. 552 (2018) 144–152, https://doi.org/10.1016/j.memsci.2018.01.069.
[35] H. Nazem-Bokaee, D. Chen, S.M. O'Donnell, A.L. Zydney, New insights into the performance characteristics of the Planova-series hollow-fiber parvovirus filters using confocal and electron microscopy, Biotechnol. Bioeng. 116 (2019) 2010–2017, https://doi.org/10.1002/bit.26991.
[36] F. Fallahianbijan, S. Giglia, C. Carbrello, D. Bell, A.L. Zydney, Impact of protein fouling on nanoparticle capture within the Viresolve® Pro and Viresolve® NFP virus removal membranes, Biotechnol. Bioeng. 116 (2019) 2285–2291, https://doi.org/10.1002/bit.27017.
[37] H. Nazem-Bokaee, D. Chen, S.M. O'Donnell, A.L. Zydney, Visualizing effects of protein fouling on capture profiles in the Planova BioEX and 20N virus filters, J. Membr. Sci. 610 (2020), https://doi.org/10.1016/j.memsci.2020.118271.
[38] F.W. Pontius, G.L. Amy, M.T. Hernandez, Fluorescent microspheres as virion surrogates in low-pressure membrane studies, J. Membr. Sci. 335 (2009) 43–50, https://doi.org/10.1016/j.memsci.2009.02.026.
[39] S. Lute, M. Bailey, J. Combs, M. Sukumar, K. Brorson, Phage passage after extended processing in small-virus-retentive filters, Biotechnol. Appl. Biochem. 47 (2007) 141, https://doi.org/10.1042/ba20060254.
[40] R. Leisi, J. Bieri, N.J. Roth, C. Ros, Determination of parvovirus retention profiles in virus filter membranes using laser scanning microscopy, J. Membr. Sci. 603 (2020), https://doi.org/10.1016/j.memsci.2020.118012.
[41] R. Leisi, R. Wolfisberg, T. Nowak, O. Caliaro, A. Hemmerle, N.J. Roth, C. Ros, Impact of the isoelectric point of model parvoviruses on viral retention in anion-exchange chromatography, Biotechnol. Bioeng. 118 (2020) 116–129, https://doi.org/10.1002/bit.27555.
[42] R. Leisi, M.V. Nordheim, C. Ros, C. Kempf, The VP1u receptor restricts parvovirus B19 uptake to permissive erythroid cells, Viruses 8 (2016), https://doi.org/10.3390/v8100265.
[43] R.P. Haugland, Coupling of monoclonal antibodies with fluorophores, Methods Mol. Biol. 45 (1995) 205–221, https://doi.org/10.1385/0-89603-308-2:205.
[44] M.A. Hobisch, J. Bossu, D. Mandlez, S.M. Bardet, S. Spirk, R. Eckhart, W. Bauer, Localization of cellulosic fines in paper via fluorescent labeling, Cellulose 26 (2019) 6933–6942, https://doi.org/10.1007/s10570-019-02556-0.
[45] C.A. Schneider, W.S. Rasband, K.W. Eliceiri, NIH Image to ImageJ: 25 years of image analysis, Nat. Methods 9 (2012) 671–675, https://doi.org/10.1038/nmeth.2089.
[46] M. Tsujikawa, Y. Ohkubo, M. Masuda, H. Tanaka, K. Takahashi, Y. Sasaki, M. Yunoki, K. Ikuta, Caution in evaluation of removal of virus by filtration: misinterpretation due to detection of viral genome fragments by PCR, J. Virol. Methods 178 (2011) 39–43, https://doi.org/10.1016/j.jviromet.2011.08.009.
[47] S. Ideno, K. Takahashi, K. Yusa, K. Sakai, Quantitative PCR evaluation of parvovirus B19 removal via nanofiltration, J. Virol. Methods 275 (2020), https://doi.org/10.1016/j.jviromet.2019.113755.
[48] M.J. Merchlinsky, P.J. Tattersall, J.J. Leary, S.F. Cotmore, E.M. Gardiner, D. C. Ward, Construction of an infectious molecular clone of the autonomous parvovirus minute virus of mice, J. Virol. 47 (1983) 227–232.
[49] H. Ruppach, Log10 reduction factors in viral clearance studies, Bioprocess J. 12 (2014) 24–30, https://doi.org/10.12665/j124.ruppach.
[50] M. Cabatingan, Impact of virus stock quality on virus filter validation, Bioprocess Int 3 (2005) 39–43.
[51] A. Slocum, M. Burnham, P. Genest, A. Venkiteshwaran, D. Chen, J. Hughes, Impact of virus preparation quality on parvovirus filter performance, Biotechnol. Bioeng. 110 (2013) 229–239, https://doi.org/10.1002/bit.24600.
[52] P. De Vilmorin, A. Slocum, T. Jaber, O. Schaefer, H. Ruppach, P. Genest, Achieving a successful scale-down model and optimized economics through parvovirus filter validation using purified TrueSpikeTM viruses, PDA J. Pharm. Sci. Technol. 69 (2015) 440–449, https://doi.org/10.5731/pdajpst.2015.01054.
[53] K. Yamaguchi, E. Miyagawa, H. Takahashi, T. Miyazaki, H. Ikeda, Electron microscopic estimation of removal of parvovirus B19 (HPVB19) by nanofiltration with a novel filter membrane, J. Membr. Sci. 298 (2007) 99–109, https://doi.org/10.1016/j.memsci.2007.04.009.
[54] T. Hongo-Hirasaki, K. Yamaguchi, K. Yanagida, H. Hayashida, S. Ide, Effects of varying virus-spiking conditions on a virus-removal filter Planova^{TM} 20N in a virus validation study of antibody solutions, Biotechnol. Prog. 27 (2011) 162–169, https://doi.org/10.1002/btpr.533.
[55] J. Adan-Kubo, M. Tsujikawa, K. Takahashi, T. Hongo-Hirasaki, K. Sakai, Microscopic visualization of virus removal by dedicated filters used in biopharmaceutical processing: impact of membrane structure and localization of captured virus particles, Biotechnol. Prog. 35 (2019), https://doi.org/10.1002/btpr.2875.
[56] S. Wang, B. Li, F. Zhang, Molecular fluorophores for deep-tissue bioimaging, ACS Cent. Sci. 6 (2020) 1302–1316, https://doi.org/10.1021/acscentsci.0c00544.
[57] P. Liu, X. Mu, X.D. Zhang, D. Ming, The near-infrared-II fluorophores and advanced microscopy technologies development and application in bioimaging, Bioconjugate Chem. 31 (2020) 260–275, https://doi.org/10.1021/acs.bioconjchem.9b00610.
[58] F. Fallahianbijan, S. Giglia, C. Carbrello, A.L. Zydney, Quantitative analysis of internal flow distribution and pore interconnectivity within asymmetric virus filtration membranes, J. Membr. Sci. 595 (2020), https://doi.org/10.1016/j.memsci.2019.117578.
[59] S.K. Dishari, A. Venkiteshwaran, A.L. Zydney, Probing effects of pressure release on virus capture during virus filtration using confocal microscopy, Biotechnol. Bioeng. 112 (2015) 2115–2122, https://doi.org/10.1002/bit.25614.
[60] C. Dika, J.F.L. Duval, G. Francius, A. Perrin, C. Gantzer, Isoelectric point is an inadequate descriptor of MS2, Phi X 174 and PRD1 phages adhesion on abiotic surfaces, J. Colloid Interface Sci. 446 (2015) 327–334, https://doi.org/10.1016/j.jcis.2014.08.055.
[61] S.A. Johnson, A. Walsh, M.R. Brown, S.C. Lute, D.J. Roush, M.S. Burnham, K. A. Brorson, The step-wise framework to design a chromatography-based hydrophobicity assay for viral particles, J. Chromatogr. B Anal. Technol. Biomed. Life Sci. 1061–1062 (2017) 430–437, https://doi.org/10.1016/j.jchromb.2017.08.002.
[62] M. Ayano, Y. Sawamura, T. Hongo-Hirasaki, T. Nishizaka, Direct visualization of virus removal process in hollow fiber membrane using an optical microscope, Sci. Rep. 11 (2021), https://doi.org/10.1038/s41598-020-78637-z.